Journal of the American Ceramic Society

RESEARCH ARTICLE OPEN ACCESS

La_2O_3-Doped ZrO_2 Tapes for Enhanced Thermomagnetic Conversion in CoFeB Heterostructures

Marcio A. Correa[1] | Nivia L. C. Siqueira[1] | Juliano C. Denardin[1,2] | Romuald T. Doumbi[1] | Artur de Morais[1] | Rodolfo B. da Silva[1] | Maurício R. D. Bomio[3] | Fabiana V. Motta[3] | Danniel F. de Oliveira[4] | Wilson Acchar[1] | Kaline P. Furlan[5] | Dachamir Hotza[6]

[1]Department of Physics (DFTE), Federal University of Rio Grande do Norte (UFRN), Natal, Rio Grande do Norte, Brazil | [2]Physics Department and CEDENNA, University of Santiago of Chile (USACH), Santiago, Chile | [3]LSQM - Laboratory of Chemical Synthesis of Materials, Department of Materials Engineering, Federal University of Rio Grande do Norte, Natal, Rio Grande do Norte, Brazil | [4]Departament of Materials Engineering (DEMAT), Federal University of Paraíba (UFPB), João Pessoa, Paraíba, Brazil | [5]Institute for Applied Materials – Ceramic Materials and Technologies (IAM-KWT), Karlsruhe Institute of Technology (KIT), Karlsruhe, Germany | [6]Department of Chemical Engineering and Food Engineering (EQA), Federal University of Santa Catarina (UFSC), Florianópolis, Santa Catarina, Brazil

Correspondence: Marcio A. Correa (marciocorrea@fisica.ufrn.br)

Received: 19 February 2026 | **Revised:** 14 May 2026 | **Accepted:** 26 May 2026

Keywords: energy conversion | La_2O_3-doped ZrO_2 | magnetron sputtering | tape casting | thermomagnetic effects

ABSTRACT

This work investigates the thermomagnetic response of La_2O_3-doped ZrO_2/CoFeB heterostructures for energy harvesting applications. La_2O_3-doped ZrO_2 ceramic tapes were fabricated via tape casting, followed by the deposition of CoFeB ferromagnetic thin films using magnetron sputtering. This combined approach enabled the realization of hybrid systems exhibiting enhanced thermoelectric performance driven by the anomalous Nernst effect (ANE). Structural characterization by scanning electron microscopy and X-ray diffraction confirmed the formation of La_2O_3-related phases in the ceramic matrix. Surface polishing improved the ceramic–ferromagnet interface, promoting the growth of soft magnetic CoFeB layers. The thermomagnetic response was evaluated by measuring the ANE under varying thermal gradients and external magnetic fields. The heterostructure with 2% La_2O_3 doping exhibited the highest performance, with an effective coefficient of 0.26 μV/K. These results demonstrate the potential of La_2O_3-doped ZrO_2/CoFeB heterostructures for thermomagnetic energy harvesting and highlight the effectiveness of this fabrication route for achieving tunable thermomagnetic responses.

1 | Introduction

Thermoelectric energy generation relies on the conversion of thermal energy into electrical energy, driven by the physical and chemical properties of materials [1–3]. Ceramic materials have been extensively explored for promoting thermoelectric conversion [4–7]. In some cases, ceramics serve as the active elements in the conversion process, typically via the Seebeck effect [8, 9]. However, the broad applicability of ceramic materials extends far beyond thermoelectric applications. Ceramics play a central role in capacitors [10, 11], dielectric [12–15], catalysts [16], refractories [17, 18], and thermal barrier coatings (TBCs) [19–22]. There are various ceramic alloys tailored for different technological applications. Among them, zirconia (ZrO_2) stands out as one of the most interesting materials for TBC applications. Zirconia is widely studied due to its remarkable physical properties, including high hardness [23], compressive strength [24], high melting point [25], and low thermal conductivity [26–28]. More recently, rare-earth-doped ceramic materials have drawn increasing attention from the scientific community due to their outstanding potential for a wide range of technological applications [29–33]. Within this context, La_2O_3-doped ZrO_2 exhibits promising properties for

applications in dielectrics [34–36], capacitors [37], and photoluminescence [38]. Moreover, La_2O_3-doped ZrO_2 is particularly interesting due to its potential to modify the thermal and electric conductivity of zirconia ceramics. Incorporating La_2O_3 into the ZrO_2 lattice can alter the distribution of internal residual stresses, leading to enhanced phonon scattering and thereby affecting the material's thermal and electric conductivity [39]. In particular, the thermal conductivity of both bare and doped ZrO_2 ceramics plays a crucial role in ceramic applications involving thermomagnetic effects.

Thermomagnetic effects are promising mechanisms for converting thermal energy into electrical energy through ferromagnetic materials [40]. Among the thermomagnetic effects explored, the anomalous Nernst effect (ANE) stands out for its high energy conversion efficiency, even under small thermal gradients [41–44]. In particular, the ANE differs from the conventional Nernst effect in the origin of the induced electric field during the measurement. While the conventional Nernst effect arises from the Lorentz force acting on charge carriers in nonmagnetic materials, the ANE originates from the magnetization of a ferromagnetic sample and is intrinsically associated with spin–orbit coupling and the Berry curvature of the electronic structure [45].

More specifically, the ANE is the generation of an electric field $\vec{E}_{ANE}$ when a thermal gradient $\vec{\nabla} T$ is imposed perpendicularly to the sample plane with magnetization $\vec{M}$. From the theoretical point of view, this field can be written as [46–48],

$$\vec{E}_{ANE} = -C_{ANE}\left(\hat{M} \times \vec{\nabla} T\right). \quad (1)$$

where $C_{ANE} = \lambda_{ANE}\ M_s\mu_o$, with M_s being the magnetization saturation, μ_o is the vacuum magnetic permeability, and λ_{ANE} is the ANE coefficient; $\hat{M}$ is the unit vector of the magnetization $\vec{M}$. When a $\vec{\nabla} T$ is applied to a magnetic conductor, thermally driven charge carriers diffuse from the hot to the cold region. In ferromagnetic materials, the presence of spin–orbit coupling and/or spontaneous magnetization leads to a transverse deflection of these carriers, analogous to the anomalous Hall effect [49–52]. As a consequence, charge accumulation occurs perpendicular to both the thermal gradient and the magnetization, giving rise to a transverse electric field ($\vec{E}_{ANE}$) [53, 54].

As observed, the ANE-induced electric field vector $\vec{E}_{ANE}$ depends on both the ferromagnetic properties of the material and the applied thermal gradient on the ferromagnetic material. Therefore, when ferromagnetic thin films are used, the choice of substrate plays a crucial role in the thermomagnetic response. The thermal conductivity of the substrate modifies the $\vec{\nabla} T$ felt by the ferromagnetic thin film. For substrates with low thermal conductivity, such as ZrO_2 materials, the $\vec{\nabla} T$ will be concentrated on the ferromagnetic thin film, leading to an enhancement of the thermomagnetic voltage. On the other hand, for substrates with high-thermal conductivity the $\vec{\nabla} T$ will quickly pass through the ferromagnetic thin film, leading to a decrease in the ANE response [55]. Ferromagnetic alloys can exhibit distinct magnetic characteristics (e.g., soft vs. hard magnetic behavior).

For practical applications, ferromagnetic materials with high saturation magnetization (M_s), low coercive field (H_c), and high magnetic permeability are required to enhance the thermomagnetic signal measured through the ANE. Therefore, the use of soft ferromagnetic materials represents one of the most effective strategies for thermoelectric energy conversion based on the ANE. In addition, the incorporation of ferromagnetic materials with tailored magnetic anisotropies provides an interesting route to achieve tunable thermomagnetic responses as a function of the external magnetic field [56].

Within this framework, the $Ni_{81}Fe_{19}$ (Permalloy) alloy is a well-established candidate for ANE studies, as it exhibits high magnetic permeability, low coercivity, and can be easily engineered to present different anisotropy configurations [57, 58]. However, Permalloy exhibits negligible magnetostrictive properties, which limit its potential for certain sensor and flexible-device applications.

In this regard, the $Co_{40}Fe_{40}B_{20}$ alloy fulfills the required magnetic criteria while also presenting significant magnetostrictive properties, making it particularly attractive for sensor and flexible-device applications [59–62]. Moreover, $Co_{40}Fe_{40}B_{20}$ exhibits low coercivity, moderate electric resistivity, and high spin polarization, which are highly desirable characteristics for thermomagnetic applications based on the ANE [59, 60, 63].

Typical ANE coefficient values reported for thin films of these alloys range from approximately 0.1–1.0 $\mu V/K$ for NiFe [64], and 0.3–1.9 $\mu V/K$ for CoFeB [47], placing them among the most promising material systems for ANE-based energy conversion.

Despite the extensive research on thermomagnetic effects in ferromagnetic thin films, their integration with functional ceramic substrates such as La-doped ZrO_2 remains essentially unexplored. In particular, to the best of our knowledge, there are no previous reports investigating the ANE in heterostructures composed of soft ferromagnetic thin films deposited on La-doped ZrO_2 ceramic substrates. Therefore, the present study introduces a new class of thermomagnetic heterostructures by combining the favorable structural and electronic properties of La-doped ZrO_2 ceramics with soft ferromagnetic layers. This approach opens a new pathway for exploring and tailoring thermomagnetic responses, providing an alternative platform for the development of ANE-based functional devices.

In this study, we go beyond the production of ceramic tapes, prepared by tape casting (TC). Here, we integrate TC and magnetron sputtering to produce ceramic/ferromagnetic heterostructures to explore the thermomagnetic effects. More specifically, we provide a systematic investigation of, structural, morphological, and dielectric properties of La_2O_3-doped ZrO_2 tapes. These ceramic tapes were used to support the deposition of $Co_{40}Fe_{40}B_{20}$ (CoFeB) thin films by magnetron sputtering, forming La_2O_3-doped ZrO_2/CoFeB heterostructures for the study of ANE.

This work addresses a key gap in the field by systematically evaluating the potential of oxide-based ceramics in thermomagnetic studies. These experimental insights enable us to assess the influence of La_2O_3 doping concentration on the thermomagnetic response, providing a deeper understanding of the substrate's

TABLE 1 | Materials and slurry formulations used for the tape casting processes.

Function	Component	Supplier	Amount (wt.%)
Solvent	Distilled water	—	26
Ceramic powder	$(ZrO_2)_{100-x}(La_2O_3)_x$	Sigma Aldrich	45
Dispersant	Triton X-114	Sigma Aldrich	1.5
Binder	Polyvinyl alcohol	Sigma Aldrich	25
Plasticizer	Glycerol	Synth	1.5
Antifoam	Liofoam	Sigma Aldrich	1.0

active role in modifying thermomagnetic behavior and advancing the design of efficient ANE-based devices.

2 | Experimental Procedure

2.1 | Preparation of Ceramic Tapes

Water-based casting formulation was employed to prepare ceramic tapes with variable compositions of $(ZrO_2)_{100-x}(La_2O_3)_x$, where x (wt.%) ranged from 0 to 3, in mass. The resulting samples were designated as Zr–Lax, with x being 0%, 1%, 2%, and 3%, in mass, respectively. For this study, we employed ZrO_2 and La_2O_3 powders obtained from Sigma Aldrich with purities of 99.99% and 99%. Initially, the ceramic powders were dispersed in distilled water, which was used as the solvent in the presence of a dispersing agent (Triton X-114). The dispersion was carried out in a container with alumina balls serving as the grinding media and subjected to ball milling for 24 h. Subsequently, the binder (polyvinyl alcohol hydrolyzed at 16.6%), plasticizer (glycerol), and antifoaming agent (Liofoam) were added to the mixture and further homogenized by ball milling for an additional 24 h. Table 1 summarizes the components used in the slurries, along with their respective functions and quantities.

The suspensions were cast using a TC machine TTC-1200 (Tape Casting Warehouse Inc.) at a casting speed of 20.2 cm/min, with the doctor blade gap set to 0.55 mm. The resulting flexible tapes were dried in situ for 24 h and subsequently cut into circular shapes. The dried sheets were then stacked and laminated into 10-layer blocks, followed by uniaxial pressing at 120 MPa for 2 min at 70°C. To remove the organic components, the samples were subjected to a thermal treatment at 600°C for 1 h, with a heating rate of 1°C/min. Subsequently, the specimens were sintered at 1250°C for 2 h and then allowed to cool naturally to room temperature. After drying, tapes with a thickness of around 200 μm were obtained.

2.2 | Structural and Morphological Characterization

The structural properties were studied through X-ray diffraction (XRD) using a Rigaku Mini-Flex II with Cu-K α radiation, in Bragg–Brentano geometry. The measurement was recorded in the range 10° to 80° (2θ), and with a step of 0.02° and scan rate of 1.5°/min. The morphological aspects were verified using a scanning electron microscope (SEM) with a field emission gun

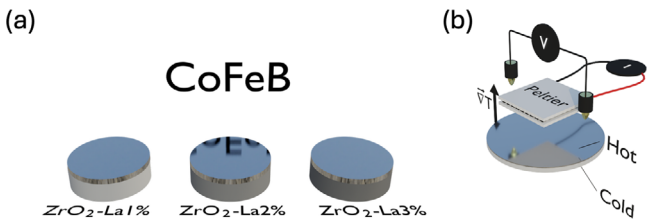

FIGURE 1 | (a) La_2O_3-doped ZrO_2/CoFeB heterostructures produced by integrating tape casting and magnetron sputtering techniques. (b) Thermomagnetic experimental setup for ANE measurements. The distance of the electric contact is ~12 mm.

(SEM-FEG) Zeiss Auriga 40 model. The elemental composition of the samples was analyzed using energy-dispersive X-ray spectroscopy (EDS) coupled with SEM-FEG equipment.

2.3 | Deposition of Thin Films

Prior to thin film deposition and after structural, morphological, and dielectric characterization, the ceramic substrates were prepared for the ferromagnetic thin film. In this case, 10 layers with circular geometry (12 mm in diameter) were considered for each composition. To improve the quality of the interface, polishing processes were performed on the ceramic substrate. In this case, a procedure similar to that applied in a previous study conducted by Neto et al. [65] was performed. The $Co_{40}Fe_{40}B_{20}$ (CoFeB) thin films with $t_f = 60$ nm were deposited using magnetron sputtering from a commercial target (99.99 purity). The target and the La_2O_3-doped ZrO_2 ceramic substrate were inserted in a chamber with base pressure of 4×10^{-6} Torr. During the depositions, a work Ar pressure of 3.0×10^{-3} Torr with a gas flux of 20 sccm were maintained in the chamber, while a DC current of 101 mA was set on the source. These deposition parameters allow reaching a deposition rate of 0.089 nm/s. Deposition onto ceramic tapes was performed on circular substrates with a 12 mm diameter, as depicted in Figure 1a. For the thin film deposited onto a glass substrate, a squared shape was considered, with 3×3 mm^2. All thin films were deposited at room temperature and without any external magnetic field.

2.4 | Magnetic and Thermomagnetic Characterizations

The magnetic properties were measured in a Vibrating Sample Magnetometer (VSM) LakeShore 7400 series. The external mag-

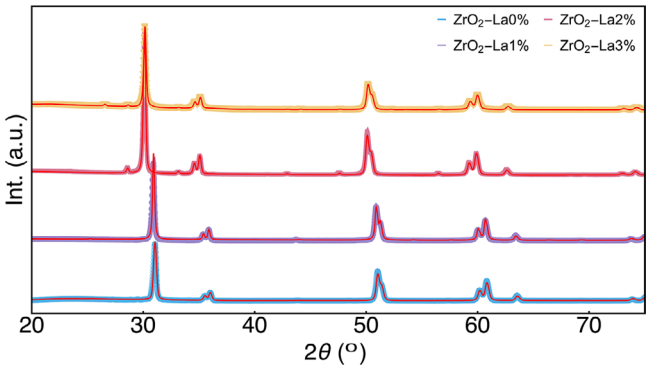

FIGURE 2 | X-ray diffraction patterns for the La-doped ZrO_2 ceramic tapes. The red line represents the best fit obtained from Rietveld refinement and phase identification. The peaks were indexed based on ICSD-85322 and ICSD-100209, for ZrO_2 and La_2O_3 phases, respectively. The plane (101) in red at $2\theta \approx 29.07°$ corresponds to the La_2O_3 phase, while the other planes in black correspond to the ZrO_2 phase.

netic field was applied in the CoFeB film plane and measured at room temperature. The samples were rotated in the field to prove the isotropic magnetic properties. The thermomagnetic properties were measured in a home-made system. In this system, the thermal gradient ($\vec{\nabla} T$) is generated by a micro-Peltier module. The micro-Peltier is responsible for heating the surface of the heterostructure, while the opposite side of it is connected to a thermal sink. Another thermal sink is connected to the bottom of the substrate, which is responsible for dissipating the thermal energy, maximizing the temperature difference (ΔT) between the top of the ferromagnetic thin film and the bottom of the ceramic substrate (see Figure 1b). The thermoelectric voltage is measured by using a high-precision $7_{1/2}$ digits multimeter model 34470A from Keysight. The thermomagnetic voltage relates to the $\vec{E}_{ANE}$ can be obtained through [46],

$$V_{ANE} = -\int_0^L \left(\vec{E} \cdot d\,\vec{l}\right), \tag{2}$$

where L is the distance between the electric contacts (12 mm in this case). The schematic representation of the experimental setup can be observed in Figure 1b. To ensure optimal thermal conductivity between the sample and the thermal sinks, a high-thermal-conductivity paste was used during the experimental setup.

3 | Results and Discussion

3.1 | Structural and Morphological Properties of La_2O_3-Doped ZrO_2 Ceramic Tapes

Figure 2 shows the XRD patterns of the La_2O_3-doped ZrO_2 ceramic tapes. The patterns were analyzed and refined using the Rietveld method in GSAS II [66]. In this case, the following parameters were refined: scale factor, background, lattice parameters, profile half-width parameters (u, v, w), atomic positions, isotropic thermal parameters, and occupancy. Based on the Rietveld refinement and phase identification (vide red line), Zr–La0% shows a single ZrO_2 phase, with tetragonal symmetry and space group *P42/nmc* (ICSD-85322).

TABLE 2 | Parameters obtained from XRD Rietveld refinement and phase identification for Zr–La0%, Zr–La1%, Zr–La2%, and Zr–La3% samples.

Material	a (Å)	c (Å)	R_{wp}	R_{exp}	R_p	χ^2	Wt
Zr–La0%	3.5986	5.1521	18%	15.2	14.6	1.40	$ZrO_2 = 100\%$
Zr–La1%	3.5986	5.1522	17%	14.1	13.4	1.45	$ZrO_2 = 87\%$
	4.0270	6.8159					$La_2O_3 = 13\%$
Zr–La2%	3.5988	5.1522	18.9%	15.5	14.7	1.49	$ZrO_2 = 83\%$
	4.0276	6.8162					$La_2O_3 = 17\%$
Zr–La3%	3.5989	5.1524	18.9%	15.4	14.5	1.50	$ZrO_2 = 81\%$
	4.0366	6.8167					$La_2O_3 = 19\%$

The samples Zr–La1%, Zr–La2%, and Zr–La3% exhibit a new peak at $2\theta \approx 29.07°$ which corresponds to La_2O_3 oxide with hexagonal symmetry and space group—*P63/mmc* (ICSD-100209). The presence of the La_2O_3 peak may be attributed to the interaction between ZrO_2 with La, leading to the formation of $ZrO_2 + La_2O_3$. The parameters obtained from Rietveld refinement are shown in Table 2.

The structural parameters obtained from the Rietveld refinement confirm that the undoped sample exhibits a single-phase ZrO_2 structure. With the introduction of La, the XRD analysis reveals the emergence of a secondary La_2O_3 phase coexisting with the ZrO_2 matrix. As the La concentration increases, a gradual increase in the weight fraction of the La_2O_3 phase is observed, accompanied by a corresponding reduction of the ZrO_2 phase fraction. This behavior indicates that only a limited amount of La can be incorporated into the zirconia lattice under the present synthesis conditions, while the excess dopant tends to segregate, forming a lanthanum oxide phase. In addition, subtle variations in the lattice parameters of both phases suggest slight structural distortions and lattice relaxation effects associated with the presence of La and the progressive formation of La_2O_3. Overall, these results indicate that La incorporation promotes the gradual development of a secondary oxide phase while only weakly affecting the crystalline framework of the ZrO_2 host structure.

Figures 3a–d show the SEM micrographs for the studied materials measured in the cross-section view. This analysis is particularly useful for evaluating the densification of our materials after the stacking, pressing, and sintering processes. These properties have a direct influence on the material's thermal conductivity, which is a key factor for thermoelectric analyses. In general, a good uniformity in densification can be observed for bare ZrO_2 (Zr–La0%,), Zr–La1%, and Zr–La3%. On the other hand, for the Zr–La2% composition, a clear formation of overlapped layers with a well-defined orientation is observed. This feature may significantly affect the sample's thermal conductivity due to interfaces between successive layers. Considering the top-view analyses, before the ferromagnetic thin film deposition, for a high magnification (see Figure 3e–h), it is observed that the presence

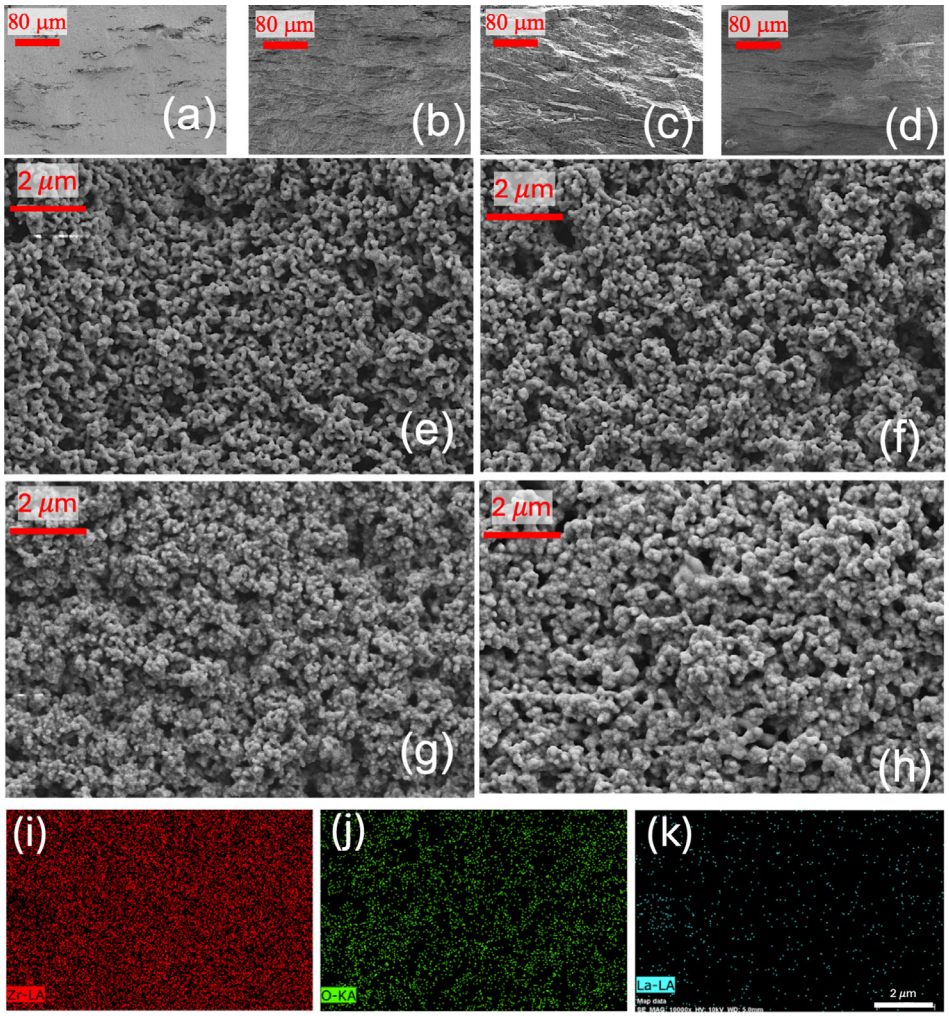

FIGURE 3 | SEM images obtained from the studied Zr–La*x* tapes. (a) Cross-section Zr–La0%, that is, for undoped ZrO_2. (b) Cross-section Zr–La1%. (c) Cross-section Zr–La2%. (d) Cross-section Zr–La3%. (e–h) Similar analyses for high magnifications to verify the porosity and grains sizes. The image is related to Zr–La0%, Zr–La1%, Zr–La2%, and Zr–La3%, respectively. (i–k) Representative color maps for the Zr–La1%. Similar elemental distributions were observed for the other compositions.

of distinct grain sizes, with irregular geometries. This feature is related to the mixing process and thermal heating during the sintering of the material [67]. At the same time, the increase in tape porosity is imperceptible. These features are essential for using these materials as substrates for ferromagnetic layers. An increase in the roughness of the substrate can induce internal stress in the ferromagnetic layer deposited, which leads to an increase of essential properties such as the magnetic coercivity [58, 68–70]. Figures 3i–k depict the EDS results (color map) for the representative Zr–La1%. As expected, the presence of the La_2O_3 is clearly detected. The EDS spectra for all samples are available in the Supporting Information.

Therefore, both XRD and SEM-EDS results confirm the successful incorporation of La_2O_3 into the ZrO_2 matrix. From this point onward, the focus shifts to magnetic and thermomagnetic characterization of the complete La_2O_3-doped ZrO_2/CoFeB heterostructures. Additionally, only La_2O_3-doped ZrO_2 samples are considered in the following discussion, as similar investigations on undoped ZrO_2 tapes have already been reported in the literature [48].

3.2 | Magnetic Characterization of La_2O_3-Doped ZrO_2/CoFeB Heterostructures

First, the normalized magnetization curves for the studied heterostructure are analyzed, as shown in Figure 4. For this study, we define M/M_s the magnetization of the material for a given set of magnetic field values (M) normalized for the maximum values of the magnetization, when the system is magnetically saturated (M_s). Here, the magnetic response of La_2O_3-doped ZrO_2/CoFeB heterostructures is compared to that of a CoFeB thin film deposited on a glass amorphous substrate (see bottom inset of Figure 4a). This comparison is essential for determining whether La_2O_3-doped ZrO_2 influences the quasi-static magnetic properties of the CoFeB layer. The coercive field is between 10 and 13 Oe for all studied heterostructures, which is typical for this alloy in thin film form [59, 71]. The magnetization curves exhibit in-plane isotropic magnetic behavior, showing similar responses for different orientations of the magnetic field applied within the film plane, as depicted in Figure 4b. In this figure, representative magnetization curves measured as a function of the external magnetic field for different in-plane angles are presented.

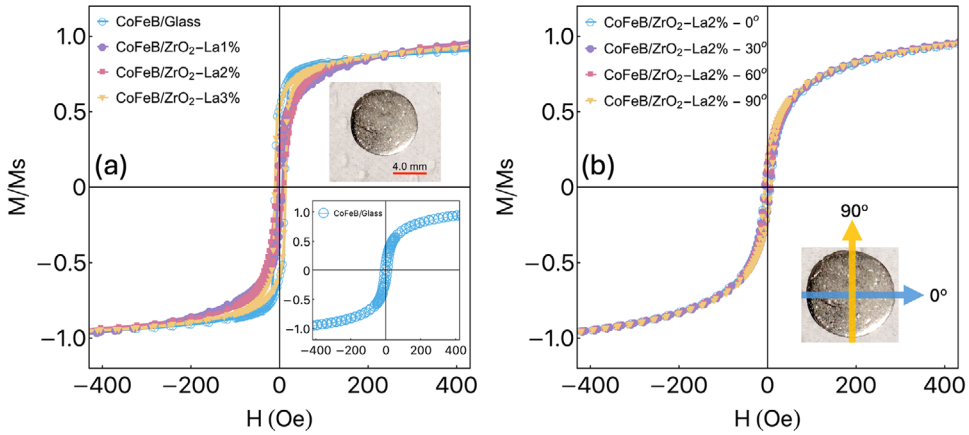

FIGURE 4 | (a) Normalized magnetization curves for the La_2O_3-doped ZrO_2/CoFeB heterostructures with the external magnetic field applied in the film plane. The top inset shows a representative La_2O_3-doped ZrO_2 tape coated with a 60 nm CoFeB thin film. The bottom inset depicts the magnetization curves for CoFeB films grown on glass substrates. (b) Representative magnetization curves as a function of the external magnetic fields for distinct angles for CoFeB/ZrO_2–La2%. The inset shows the angle definitions for the external magnetic field applied to the film plane.

These measurements were performed for the CoFeB/ZrO_2–La2% heterostructure. Notably, all substrates, including the glass amorphous substrate, produce similar magnetic responses. With a similar coercive field H_c. On the other hand, for the saturation field H_s values the glass substrate presents a value of around 30 Oe, while for the CFB thin film growth onto ceramic substrates these values increase to around 50 Oe. This consistent magnetic behavior across different substrates is crucial, as it enables a direct comparison of their thermomagnetic responses. Since the magnetization curves remain unchanged, any observed differences in thermomagnetic behavior can be attributed primarily to variations in thermal conductivity and morphological characteristics of the La_2O_3-doped ZrO_2 tapes.

3.3 | Thermomagnetic Response and ANE Coefficient Extraction

For the thermomagnetic characterization, the vector configuration of the magnetization ($\vec{M}$) and the thermal gradient ($\vec{\nabla} T$), with module of ΔT, are depicted in Figure 5a. This configuration is designed to maximize the thermomagnetic voltage (V), as the induced electric field ($\vec{E}_{ANE}$) aligns with the direction of the electric contacts, as described by Equation (2). Moreover, to obtain the $V_{ANE} \times \Delta T$ dependence, which provides important information on the thermoelectric energy conversion, the Peltier module was operated at distinct current levels (0–500 mA). This generates distinct values of ΔT, which is the temperature difference between the top and bottom of the La_2O_3-doped ZrO_2/CoFeB heterostructure. Figure 5b shows the thermomagnetic voltage of a representative CoFeB/Zr–La2% heterostructure. Similar results, with distinct thermomagnetic voltage levels, were observed for other La concentrations. For $\Delta T = 0$ K, no thermomagnetic voltage was observed, as expected (see Equation 1). On the other hand, by increasing ΔT, an increase of the induced thermomagnetic voltage was noticed in the system. Although with a lower signal/noise ratio, the shape of the voltage curves closely resembles the magnetization curves presented in Figure 4. To emphasize this correspondence, Figure 5c displays the normalized magnetization and thermomagnetic measurements for CoFeB/Zr–La2% submitted at $\Delta T = 16$ K. The strong similarity between the two curves confirms the reliability and effectiveness of the ANE measurements.

According to Equation (1), the maximum voltage (V_{ANE}^{max}), for a magnetically saturated material, is expected to exhibit a linear dependence on the applied temperature gradient ($\vec{\nabla} T$). The slope of this linear relationship reveals the efficiency of thermoelectric energy conversion of a given heterostructure, in which both the ferromagnetic thin film and the substrate should be considered. This slope is named as the effective coefficient (C_{eff}). While the CoFeB layer is the active component where ANE occurs, the ceramic substrate influences the effective temperature difference across the film (ΔT_f) due to its thermal conductivity. In this study, a low La_2O_3 concentration was selected to enable an initial investigation of the ANE in this kind of heterostructure. This reduced concentration was chosen to minimize changes in the intrinsic properties of the ceramic matrix, allowing us to verify whether the ANE could be detected and reliably measured in this system.

Figure 5d shows the V_{ANE}^{max} as a function of the ΔT for the heterostructure studied. The expected linear behavior is verified for all systems. The C_{eff} reached values of 0.18 μV/K, 0.26 μV/K, and 0.20 μV/K, for the heterostructures with 1%, 2%, and 3% of La doping, respectively.

To extract C_{ANE} from experimental parameters, the following relation should be considered [46, 72],

$$C_{ANE} = \frac{V_{ANE}^{max} t_f}{L \Delta T_f}, \tag{3}$$

with ΔT_f the temperature difference between the top and bottom of the thin ferromagnetic film, given by [72]

$$\Delta T_f = \frac{t_f \kappa_S}{t_S \kappa_f} \Delta T \tag{4}$$

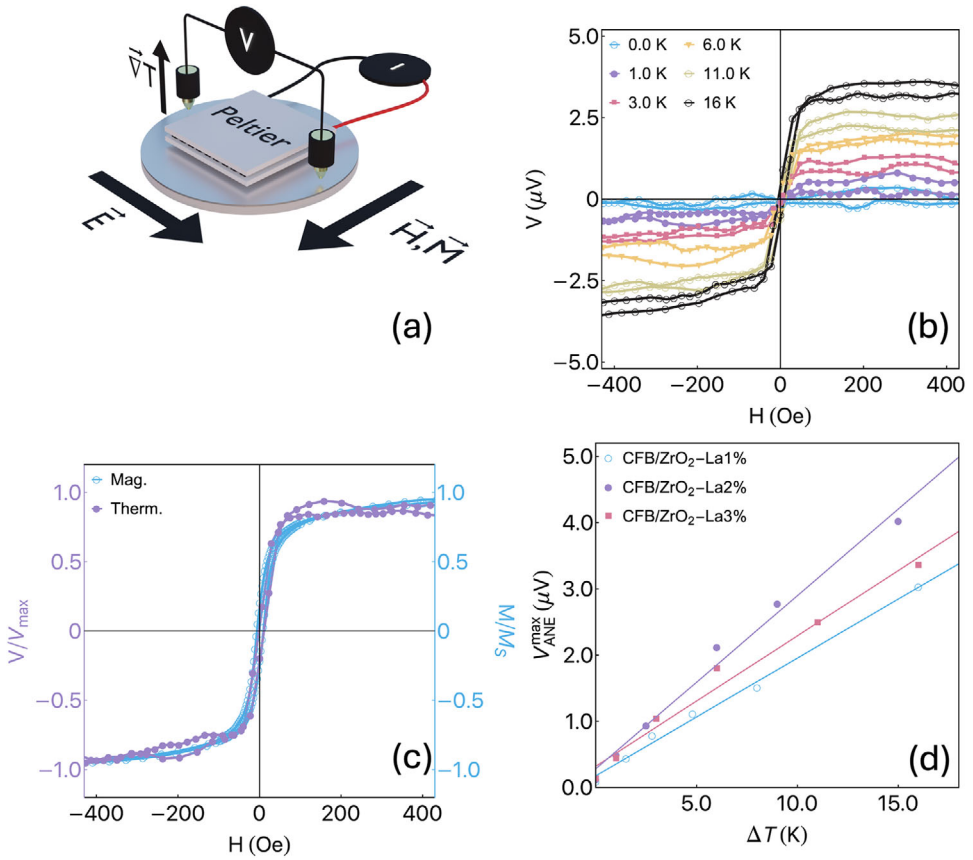

FIGURE 5 | (a) Vector configuration of magnetization and thermal gradient during the thermomagnetic measurements. The thermal gradient $\vec{\nabla} T$ with modulus ΔT is applied between the top of the thin film and the bottom of the ceramic substrate. (b) Thermomagnetic voltage as a function of the external magnetic field for distinct ΔT values. (c) Comparison between thermomagnetic voltage and magnetization curve for the representative CoFeB/Zr–La2% heterostructure. (d) $V_{\mathrm{ANE}}^{\mathrm{max}}$ as a function of ΔT for the studied heterostructures.

where κ_S is the thermal conductivity of the ceramic substrate with thickness t_S, and κ_f the thermal conductivity of the CoFeB thin film with thickness t_f. It is important to point out that the temperature difference across the thin film (ΔT_f) is considerably smaller than the overall temperature difference across the entire heterostructure. This is primarily due to the considerable difference between the thicknesses of the thin film and the ceramic substrate. In summary, the C_{eff} reflects the thermoelectric energy conversion efficiency of the full heterostructure and serves as a practical thermo-to-electric energy conversion application. In contrast, C_{ANE} is an intrinsic property of the ferromagnetic alloy and is used to validate the experimental results with respect to the material's ANE response.

Regarding C_{eff}, it is essential to consider the thermal conductivities of both the ceramic substrate and the ferromagnetic metallic thin film. In this case, the structural properties, specifically the polycrystalline nature of the La_2O_3-doped ZrO_2 ceramic substrate and the CoFeB thin film, play a central role in determining the final thermal conductivity. For composites and polycrystalline ceramic materials with multiple phases, as observed in this study, the rule of mixtures can be applied to estimate the overall thermal conductivity [73].

The rule of mixtures assumes that the overall thermal transport results from the weighted contribution of each constituent phase. In this approach, the effective thermal conductivity of the system is obtained by combining the thermal conductivities of the individual phases according to their respective volume or weight fractions [74, 75]. Thus, phases with higher thermal conductivity contribute proportionally more to the overall heat transport, while phases with lower conductivity tend to reduce the effective value of the composite. Although this method provides only an approximate description, it is widely used as a first-order estimation for polycrystalline ceramics and multiphase systems, where heat transport is primarily governed by phonon propagation and scattering at grain boundaries and phase interfaces. In the present case, this approach allows a reasonable estimation of the effective thermal conductivity of the La_2O_3–ZrO_2 ceramic substrate by considering the relative fractions of the ZrO_2 and La_2O_3 phases obtained from the Rietveld refinement. Table 3 shows the estimated thermal conductivity (κ) for the ceramic substrates (κ_s) and the thin film (κ_f), as well as the respective thicknesses [76–78]. Using these parameters in Equation (4), it is possible to calculate the temperature difference across the CoFeB thin film (ΔT_f). At the same time, the anomalous Nernst coefficient (C_{ANE}) of the material can be estimated using Equation (3).

Figure 6 depicts the behavior of C_{ANE} and C_{eff} as a function of La% content. A small increase in C_{eff} is observed for the CoFeB/Zr–La2% heterostructure, which correlates to the modification

TABLE 3 | Estimated thermal conductivity (κ) and thickness of La_2O_3-doped ZrO_2 ceramics and CoFeB thin film components. The nominal values of thermal conductivity were obtained in the references [76–78].

Material	Comp. (wt.%)	κ (W/m·K)	κ (W/m·K)	Thickness
ZrO_2–La1%	87% ZrO_2 13% La_2O_3	$ZrO_2 \approx 2.0$ $La_2O_3 \approx 4.0$	2.26	0.58 mm
ZrO_2–La2%	83% ZrO_2 17% La_2O_3	$ZrO_2 \approx 2.0$ $La_2O_3 \approx 4.0$	2.34	0.59 mm
ZrO_2–La3%	81% ZrO_2 19% La_2O_3	$ZrO_2 \approx 2.0$ $La_2O_3 \approx 4.0$	2.38	0.45 mm
$Co_{40}Fe_{40}B_{20}$	40% Co 40% Fe 20% B	Co ≈ 100 Fe ≈ 80 B ≈ 27	86.7	60.0 nm

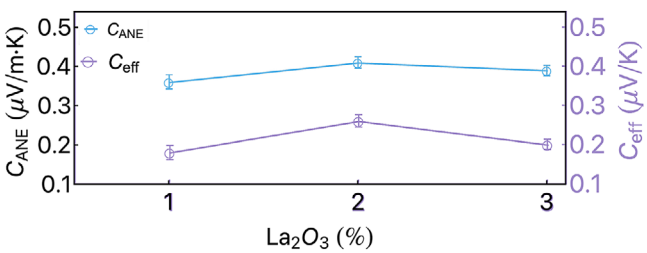

FIGURE 6 | Anomalous Nernst effect coefficient as a function of the La content in the La_2O_3-doped ZrO_2/CoFeB heterostructures.

of the cross-section structure verified in the SEM analyses. Conversely, a slight decrease in C_{ANE} is noted, likely due to interfacial modifications between the ceramic substrate and the CoFeB thin film. It is important to point out that for this analysis, we intentionally used the theoretical thermal conductivity values reported in Table 3 as reference values to calculate the ANE coefficient (C_{ANE}), ensuring a consistent and comparable analysis across all samples. However, it is important to highlight that small structural modifications (observed in SEM and XRD) are sufficient to deviate these theoretical values in practical applications, which explains the modifications observed in our values, especially for the sample with a La_2O_3 doping level of 2%.

These findings confirm the successful integration of ceramic substrates and thin ferromagnetic films to generate functional heterostructures suitable for thermoelectric energy conversion applications.

The mean value obtained for C_{eff} was approximately 0.26 μV/K (C_{ANE} = 0.38 μV/m K), which is consistent with values reported in the literature [46]. To compare our findings with the literature it is important to point out that the comparison should be related to Co-based alloys, since the magnetic properties are fundamental for the thermomagnetic response. Within this context, it is observed a wide range of values for the C_{eff} and/or C_{ANE}. For $Co_2Ti_{0.6}V_{0.4}Sn$ values of around 1.8 μV/K was observed at 220 K [51]. On the other hand, for the Co/Pt multilayer, the reported values were 0.9 μV/K. Considering a very similar CoFeB alloy, Gamino et al. [47] investigated bare CoFeB thin films as well as CoFeB/nonmagnetic metal (Pd, Ta, and Ru). For the bare CoFeB thin film, C_{ANE} reached around 1.95 $\mu V/K$. On the other hand, for the CoFeB/Pd, CoFeB/Ta and CoFeB/Ru bilayers values of 0.36 μV/K, 0.92 μV/K, and 0.14 μV/K were reported, respectively [47].

4 | Conclusions

This study fills an important gap in the field of thermoelectric and thermomagnetic materials by introducing La_2O_3-doped ZrO_2 ceramic tapes as functional substrates for ANE-based heterostructures, an approach not extensively explored in the literature. While previous studies have focused largely on metallic or semiconductor substrates, our results demonstrate that oxide-based ceramics, fabricated via scalable aqueous TC, can be effectively integrated with ferromagnetic thin films for thermoelectric applications.

The La_2O_3-doped ZrO_2 substrates exhibited tunable structural and dielectric properties (see the Supporting Information) depending on the La content. When combined with $Co_{40}Fe_{40}B_{20}$ thin films deposited by magnetron sputtering, these substrates enabled the formation of high-quality heterostructures with uniform growth and preserved magnetic behavior.

Thermomagnetic measurements confirmed the presence and reproducibility of the ANE, with the effective coefficient (C_{eff}) reaching 0.26 μV/K (C_{ANE} = 0.38 μV/m K), in agreement with reported values for CoFeB. Additionally, the effective conversion coefficient revealed how substrate composition, particularly the presence of La phases, influences the thermal-to-electric response. Overall, this work not only demonstrates the viability of La_2O_3-doped ceramic substrates for thermomagnetic applications but also establishes a versatile platform for engineering oxide/ferromagnetic interfaces in next-generation energy conversion devices.

Acknowledgments

This work was supported by the Coordination for the Improvement of Higher Education Personnel (CAPES) and the National Council for Scientific and Technological Development (CNPq). M. A. Correa acknowledges support from the National Institute of Spintronics and Advanced Magnetic Nanostructures (INCT-SpinNanoMag), as well as the following CNPq research grants: CNPq 301343/2025-0, CNPq 404353/2024-0, CNPq 400879/2025-5, and CNPq 445104/2024-4.

The Article Processing Charge for the publication of this research was funded by the Coordenação de Aperfeiçoamento de Pessoal de Nível Superior - Brasil (CAPES) (ROR identifier: 00x0ma614).

Ethics Statement

The authors have nothing to report.

Conflicts of Interest

The authors declare no conflicts of interest.

Data Availability Statement

All relevant data are within the manuscript and available from the corresponding author upon request.

References

1. D. Champier, "Thermoelectric Generators: A Review of Applications," *Energy Conversation and Management* 140 (2017): 167–181, https://doi.org/10.1016/j.enconman.2017.02.070.

2. A. Bali, R. Chetty, and R. C. Mallik, "Thin Film Thermoelectric Materials for Sensor Applications: An Overview," in *Thin Film Structures in Energy Applications* (Springer International Publishing, 2015), 215–241, https://doi.org/10.1007/978-3-319-14774-1_7.

3. Y. Zhao, L. Liu, F. Zhang, C. Di, and D. Zhu, "Advances in Organic Thermoelectric Materials and Devices for Smart Applications," *SmartMat* 2 (2021): 426–445, https://doi.org/10.1002/smm2.1034.

4. Y. Zhang, Y. Bao, D. Zhang, and C. R. Bowen, "Porous PZT Ceramics With Aligned Pore Channels for Energy Harvesting Applications," *Journal of the American Ceramic Society* 98 (2015): 2980–2983, https://doi.org/10.1111/jace.13797.

5. I. Seo, Y. Cha, I. Kang, et al., "High Energy Density Piezoelectric Ceramics for Energy Harvesting Devices," *Journal of the American Ceramic Society* 94 (2011): 3629–3631, https://doi.org/10.1111/j.1551-2916.2011.04817.x.

6. V. E. Ogbonna, A. P. I. Popoola, and O. M. Popoola, "Piezoelectric Ceramic Materials on Transducer Technology for Energy Harvesting: A Review," *Frontiers in Energy Research* 10 (2022): 1051081, https://doi.org/10.3389/fenrg.2022.1051081.

7. K. Koumoto, R. Funahashi, E. Guilmeau, et al., "Thermoelectric Ceramics for Energy Harvesting," *Journal of the American Ceramic Society* 96 (2013): 1–23, https://doi.org/10.1111/jace.12076.

8. Y. Xing, Q. Sun, and J. Wang, "Nernst and Seebeck Effects in a Graphene Nanoribbon," *Physical Review B* 80 (2009): 235411, https://doi.org/10.1103/PhysRevB.80.235411.

9. A. W. Van Herwaarden and P. M. Sarro, "Thermal Sensors Based on the Seebeck Effect," *Sensors and Actuators* 10 (1986): 321–346, https://doi.org/10.1016/0250-6874(86)80053-1.

10. J. Qi, M. Zhang, Y. Chen, et al., "High-Entropy Assisted $BaTiO_3$-Based Ceramic Capacitors for Energy Storage," *Cell Reports Physical Science* 3 (2022): 101110, https://doi.org/10.1016/j.xcrp.2022.101110.

11. Y. B. Adediji, A. M. Adeyinka, D. I. Yahya, and O. V. Mbelu, "A Review of Energy Storage Applications of Lead-Free $BaTiO_3$-Based Dielectric Ceramic Capacitors," *Energy, Ecology Environment* 8 (2023): 401–419, https://doi.org/10.1007/s40974-023-00286-5.

12. S. A. N. França, W. Acchar, S. L. A. Dantas, et al., "Enhanced High-Frequency Dielectric Properties in ZrO_2–$BaTiO_3$ Ceramic Heterostructures," *Ceramics International* 49 (2023): 36025–36030, https://doi.org/10.1016/j.ceramint.2023.08.282.

13. A. I. Y. Tok, F. Y. C. Boey, and M. K. A. Khor, "Tape Casting of High Dielectric Ceramic Substrates for Microelectronics Packaging," *Journal of Materials Engineering and Performance* 8 (1999): 469–472, https://doi.org/10.1361/105994999770346783.

14. A. A. Hendi and F. Yakuphanoglu, "Dielectric and Ferroelectric Properties of the Graphene Doped Hydroxyapatite Ceramics," *Journal of Molecular Structure* 1207 (2020): 127734, https://doi.org/10.1016/j.molstruc.2020.127734.

15. A. I. Y. Tok, F. Y. C. Boey, and K. A. Khor, "Tape Casting of High Dielectric Ceramic Composite Substrates for Microelectronics Application," *Journal of Materials Processing Technology* 89–90 (1999): 508–512, https://doi.org/10.1016/S0924-0136(99)00131-4.

16. E. Antolini and E. R. Gonzalez, "Ceramic Materials as Supports for Low-Temperature Fuel Cell Catalysts," *Solid State Ion* 180 (2009): 746–763, https://doi.org/10.1016/j.ssi.2009.03.007.

17. W. Wang, L. Xue, T. Zhang, L. Zhou, J. Chen, and Z. Pan, "Thermodynamic Corrosion Behavior of Al_2O_3, ZrO_2 and MgO Refractories in Contact With High Basicity Refining Slag," *Ceramics International* 45 (2019): 20664–20673, https://doi.org/10.1016/j.ceramint.2019.07.049.

18. R. Kusiorowski, "MgO-ZrO_2 Refractory Ceramics Based on Recycled Magnesia-Carbon Bricks," *Construction & Building Materials* 231 (2020): 117084, https://doi.org/10.1016/j.conbuildmat.2019.117084.

19. Q. Li, X. Cui, Y. Jing, et al., "Multi-Interface Modification Induced Crack Deflection Behavior and Enhanced Fracture Resistance in Thermal Barrier Coatings," *Journal of Alloys and Compounds* 1031 (2025): 181027, https://doi.org/10.1016/j.jallcom.2025.181027.

20. Q. Liu, S. Huang, and A. He, "Composite Ceramics Thermal Barrier Coatings of Yttria Stabilized Zirconia for Aero-Engines," *Journal of Materials Science and Technology* 35 (2019): 2814–2823, https://doi.org/10.1016/j.jmst.2019.08.003.

21. K. An, K. S. Ravichandran, R. E. Dutton, and S. L. Semiatin, "Microstructure, Texture, and Thermal Conductivity of Single-Layer and Multilayer Thermal Barrier Coatings of Y_2O_3-Stabilized ZrO_2 and Al_2O_3 Made by Physical Vapor Deposition," *Journal of the American Ceramic Society* 82 (1999): 399–406, https://doi.org/10.1111/j.1551-2916.1999.tb20076.x.

22. Y. S. Tian, C. Z. Chen, D. Y. Wang, and Q. Ji, "Recent Developments in Zirconia Thermal Barrier Coatings," *Surface Review and Letters* 12 (2005): 369–378, https://doi.org/10.1142/S0218625X05007207.

23. F. H. Margha, S. A.-H. M. Abdel-Hameed, N. A. E.-S. Ghonim, et al., "Crystallization Behaviour and Hardness of Glass Ceramics Rich in Nanocrystals of ZrO_2," *Ceramics International* 35 (2009): 1133–1137, https://doi.org/10.1016/j.ceramint.2008.05.009.

24. L. Hu and C.-A. Wang, "Effect of Sintering Temperature on Compressive Strength of Porous Yttria-Stabilized Zirconia Ceramics," *Ceramics International* 36 (2010): 1697–1701, https://doi.org/10.1016/j.ceramint.2010.03.009.

25. M. H. Bocanegra-Bernal and S. D. de la Torre, "Phase Transitions in Zirconium Dioxide and Related Materials for High Performance Engineering Ceramics," *Journal of Materials Science* 37 (2002): 4947–4971, https://doi.org/10.1023/A:1021099308957.

26. L. Hu, C.-A. Wang, and Y. Huang, "Porous Yttria-Stabilized Zirconia Ceramics With Ultra-Low Thermal Conductivity," *Journal of Materials Science* 45 (2010): 3242–3246, https://doi.org/10.1007/s10853-010-4331-9.

27. J. Wu, N. P. Padture, P. G. Klemens, et al., "Thermal Conductivity of Ceramics in the ZrO_2-$GdO_{1.5}$ System," *Journal of Materials Research* 17 (2002): 3193–3200, https://doi.org/10.1557/JMR.2002.0462.

28. Z.-Y. Deng, J. M. F. Ferreira, Y. Tanaka, and Y. Isoda, "Microstructure and Thermal Conductivity of Porous ZrO_2 Ceramics," *Acta Materialia* 55 (2007): 3663–3669, https://doi.org/10.1016/j.actamat.2007.02.014.

29. S. Sameshima, T. Ichikawa, M. Kawaminami, and Y. Hirata, "Thermal and Mechanical Properties of Rare Earth-Doped Ceria Ceramics," *Materials Chemistry and Physics* 61 (1999): 31–35, https://doi.org/10.1016/S0254-0584(99)00109-1.

30. C. Wang, M. Zinkevich, and F. Aldinger, "Phase Diagrams and Thermodynamics of Rare-Earth-Doped Zirconia Ceramics," *Pure and Applied Chemistry* 79 (2007): 1731–1753, https://doi.org/10.1351/pac200779101731.

31. Y. Yao, W. Liu, Y. Chan, C. Leung, C. Mak, and B. Ploss, "Studies of Rare-Earth-Doped $BiFeO_3$ Ceramics," *International Journal of Applied Ceramic Technology* 8 (2011): 1246–1253, https://doi.org/10.1111/j.1744-7402.2010.02577.x.

32. M. K. Hossain, G. A. Raihan, M. A. Akbar, et al., "Current Applications and Future Potential of Rare Earth Oxides in Sustainable Nuclear, Radiation, and Energy Devices: A Review," *ACS Applied Electronic Materials* 4 (2022): 3327–3353, https://doi.org/10.1021/acsaelm.2c00069.

33. Anil, R. Sankar, and S. K. Barbar, "Exploration of the Impact of Rare Earth Elements (Nd, Sm, Gd, and Dy) Doping on Promising Properties of Co_2SiO_4 Ceramics for Their Use in Power Electronic Modules and Luminescent Devices," *Journal of Alloys and Compounds* 1051 (2026): 186028, https://doi.org/10.1016/j.jallcom.2026.186028.

34. H. Cai, K. Tuokedaerhan, Z. Lu, R. Zhang, and H. Du, "Interface Tuning and Electrical Property Optimization of La-Doped ZrO_2 Gate

Dielectric Based on Solution Driving," *Vacuum* 217 (2023): 112542, https://doi.org/10.1016/j.vacuum.2023.112542.

35. J. Jeong, Y. Han, and H. Sohn, "Effect of La Doping on Dielectric Constant and Tetragonality of ZrO_2 Thin Films Deposited by Atomic Layer Deposition," *Journal of Alloys and Compounds* 927 (2022): 166961, https://doi.org/10.1016/j.jallcom.2022.166961.

36. X. Chou, J. Zhai, and X. Yao, "Relaxor Behavior and Dielectric Properties of La_2O_3-Doped Barium Zirconium Titanate Ceramics for Tunable Device Applications," *Materials Chemistry and Physics* 109 (2008): 125–130, https://doi.org/10.1016/j.matchemphys.2007.11.005.

37. J. Li, J. Zhou, W. Yan, et al., "Nonvolatile Applications and Reliability Investigation of La-Doped ZrO_2 Antiferroelectric Capacitors," *Electronics (Basel)* 14 (2025): 1794, https://doi.org/10.3390/electronics14091794.

38. W. S. C. de Sousa, D. M. A. Melo, J. E. C. da Silva, R. S. Nasar, M. C. Nasar, and J. A. Varela, "Photoluminescence in ZrO_2 Doped With Y and La," *Cerâmica* 53 (2007): 99–103, https://doi.org/10.1590/S0366-69132007000100015.

39. H. Zhou and D. Yi, "Effect of Rare Earth Doping on Thermo-Physical Properties of Lanthanum Zirconate Ceramic for Thermal Barrier Coatings," *Journal of Rare Earths* 26 (2008): 770–774, https://doi.org/10.1016/S1002-0721(09)60002-8.

40. M. Mizuguchi and S. Nakatsuji, "Energy-Harvesting Materials Based on the Anomalous Nernst Effect," *Science and Technology of Advanced Materials* 20 (2019): 262–275, https://doi.org/10.1080/14686996.2019.1585143.

41. T. C. Chuang, P. L. Su, P. H. Wu, and S. Y. Huang, "Enhancement of the Anomalous Nernst Effect in Ferromagnetic Thin Films," *Physical Review B* 96 (2017): 174406, https://doi.org/10.1103/PhysRevB.96.174406.

42. T. Asaba, V. Ivanov, S. M. Thomas, et al., "Colossal Anomalous Nernst Effect in a Correlated Noncentrosymmetric Kagome Ferromagnet," *Science Advances* 7 (2021): abf1467, https://doi.org/10.1126/sciadv.abf1467.

43. P. Sheng, T. Fujita, and M. Mizuguchi, "Anomalous Nernst Effect in $Co_x(MgO)_{1-x}$ Granular Thin Films," *Applied Physics Letters* 116 (2020): 142403, https://doi.org/10.1063/1.5140461.

44. Y. Sakuraba, K. Hasegawa, M. Mizuguchi, et al., "Anomalous Nernst Effect in L10-FePt/MnGa Thermopiles for New Thermoelectric Applications," *Applied Physics Express* 6 (2013): 033003, https://doi.org/10.7567/APEX.6.033003.

45. V. Vargiamidis, P. Vasilopoulos, and M. Tahir, "Neophytou, Berry Curvature, Orbital Magnetization, and Nernst Effect in Biased Bilayer WSe_2," *Physical Review B* 102 (2020): 235426, https://doi.org/10.1103/PhysRevB.102.235426.

46. A. S. Melo, A. B. de Oliveira, C. Chesman, R. D. Della Pace, F. Bohn, and M. A. Correa, "Anomalous Nernst Effect in Stressed Magnetostrictive Film Grown Onto Flexible Substrate," *Scientific Reports* 9 (2019): 15338, https://doi.org/10.1038/s41598-019-51971-7.

47. M. Gamino, J. G. S. Santos, A. L. R. Souza, et al., "Longitudinal Spin Seebeck Effect and Anomalous Nernst Effect in CoFeB/Non-Magnetic Metal Bilayers," *Journal of Magnetism and Magnetic Materials* 527 (2021): 167778, https://doi.org/10.1016/j.jmmm.2021.167778.

48. N. L. C. Siqueira, A. Morais, J. P. M. de Oliveira, et al., "Enhancing Thermoelectric Effect With $BaTiO_3$-Doped ZrO_2 Tapes and Ferromagnetic Nanostructures," *Journal of the European Ceramic Society* 44 (2024): 116787, https://doi.org/10.1016/j.jeurceramsoc.2024.116787.

49. N. Nagaosa, J. Sinova, S. Onoda, A. H. MacDonald, and N. P. Ong, "Anomalous Hall Effect," *Review of Modern Physics* 82 (2010): 1539–1592, https://doi.org/10.1103/RevModPhys.82.1539.

50. S. Meyer, R. Schlitz, S. Geprägs, et al., "Anomalous Hall Effect in YIG|Pt Bilayers," *Applied Physics Letters* 106 (2015): 132402, https://doi.org/10.1063/1.4916342.

51. J. Hu, B. Ernst, S. Tu, et al., "Anomalous Hall and Nernst Effects in Co_2TiV and $Co_2Ti_{0.6}V_{0.4}Sn$ Heusler Thin Films," *Physical Review Applied* 10 (2018): 044037, https://doi.org/10.1103/PhysRevApplied.10.044037.

52. Z. Zhu, S. W. Or, and G. Wu, "Anomalous Hall Effect in Quarternary Heusler-Type $Ni_{50}Mn_{17}Fe_8Ga_{25}$ Melt-Spun Ribbons," *Applied Physics Letters* 95 (2009): 032503, https://doi.org/10.1063/1.3176479.

53. C. Sun, S. M. Rafi-Ul-Islam, H. Yang, and M. B. A. Jalil, "Spin Nernst and Anomalous Nernst Effects and Their Signature Outputs in Ferromagnet/Nonmagnet Heterostructures," *Physical Review B* 102 (2020): 214419, https://doi.org/10.1103/PhysRevB.102.214419.

54. T. Kikkawa, K. Uchida, S. Daimon, et al., "Separation of Longitudinal Spin Seebeck Effect From Anomalous Nernst Effect: Determination of Origin of Transverse Thermoelectric Voltage in Metal/Insulator Junctions," *Physical Review B* 88 (2013): 214403, https://doi.org/10.1103/PhysRevB.88.214403.

55. J. Alvarez-Quintana, "Impact of the Substrate on the Efficiency of Thin Film Thermoelectric Technology," *Applied Thermal Engineering* 84 (2015): 206–210, https://doi.org/10.1016/j.applthermaleng.2015.03.062.

56. M. A. Correa, M. Gamino, A. S. de Melo, et al., "Unraveling the Role of Magnetic Anisotropy on the Thermoelectric Response: A Theoretical and Experimental Approach," *Journal of Physics D Applied Physics* 55 (2022): 025001, https://doi.org/10.1088/1361-6463/ac29e4.

57. J. Ben Youssef, N. Vukadinovic, D. Billet, and M. Labrune, "Thickness-Dependent Magnetic Excitations in Permalloy Films With Nonuniform Magnetization," *Physical Review B* 69 (2004): 174402.

58. E. F. Silva, M. A. Corrêa, R. D. Della Pace, et al., "Thickness Dependence of the Magnetic Anisotropy and Dynamic Magnetic Response of Ferromagnetic NiFe Films," *Journal of Physics D Applied Physics* 50 (2017): 185001, https://doi.org/10.1088/1361-6463/aa6665.

59. R. Sun, Y. Li, Z. K. Xie, et al., "Determination of Spin Pumping Effect in CoFeB/Ir Bilayer," *Journal of Magnetism and Magnetic Materials* 497 (2020): 165971, https://doi.org/10.1016/j.jmmm.2019.165971.

60. H. Q. Tu, B. Liu, D. W. Huang, et al., "Gilbert Damping in CoFeB/GaAs(001) Film With Enhanced In-Plane Uniaxial Magnetic Anisotropy," *Scientific Reports* 7 (2017): 43971, https://doi.org/10.1038/srep43971.

61. H. Ulrichs, B. Lenk, and M. Münzenberg, "Magnonic Spin-Wave Modes in CoFeB Antidot Lattices," *Applied Physics Letters* 97 (2010): 092506, https://doi.org/10.1063/1.3483136.

62. M. Gueye, F. Zighem, M. Belmeguenai, M. S. Gabor, C. Tiusan, and D. Faurie, "Spectroscopic Investigation of Elastic and Magnetoelastic Properties of CoFeB Thin Films," *Journal of Physics D Applied Physics* 49 (2016): 145003, https://doi.org/10.1088/0022-3727/49/14/145003.

63. N. Liebing, S. Serrano-Guisan, K. Rott, et al., "Determination of Spin-Dependent Seebeck Coefficients of CoFeB/MgO/CoFeB Magnetic Tunnel Junction Nanopillars," *Journal of Applied Physics* 111 (2012): 07C520, https://doi.org/10.1063/1.3679769.

64. K. Uchida, T. Ota, H. Adachi, et al., "Thermal Spin Pumping and Magnon-Phonon-Mediated Spin-Seebeck Effect," *Journal of Applied Physics* 111 (2012): 103903, https://doi.org/10.1063/1.4716012.

65. J. M. D. Neto, A. de Morais, R. T. Doumbi, et al., "Enhancing the Electric, Dielectric and Magnetic Properties of $TiNb_2O_7$/NiFe Heterostructures," *Ceramics International* 51 (2025): 9312–9319, https://doi.org/10.1016/j.ceramint.2024.12.366.

66. B. H. Toby and R. B. Von Dreele, "GSAS-II : The Genesis of a Modern Open-Source all Purpose Crystallography Software Package," *Journal of Applied Crystallography* 46 (2013): 544–549, https://doi.org/10.1107/S0021889813003531.

67. H. P. A. Alves, A. C. S. Costa, M. A. Correa, F. Bohn, R. D. Della Pace, and W. Acchar, "Structural, Magnetic and Electric Properties of ZrO_2 Tapes Decorated With Magnetic Nanoparticles," *Ceramics International* 45 (2019): 14500–14504, https://doi.org/10.1016/j.ceramint.2019.04.123.

68. Y.-P. Zhao, R. M. Gamache, G.-C. Wang, T.-M. Lu, G. Palasantzas, and J. T. M. De Hosson, "Effect of Surface Roughness on Magnetic Domain Wall Thickness, Domain Size, and Coercivity," *Journal of Applied Physics* 89 (2001): 1325–1330, https://doi.org/10.1063/1.1331065.

69. M. Belusky, S. Lepadatu, J. Naylor, and M. M. Vopson, "Evidence of Substrate Roughness Surface Induced Magnetic Anisotropy in $Ni_{80}Fe_{20}$ Flexible Thin Films," *Journal of Magnetism and Magnetic Materials* 478 (2019): 77–83, https://doi.org/10.1016/j.jmmm.2019.01.097.

70. S. J. Steinmuller, C. A. F. Vaz, V. Ström, et al., "Effect of Substrate Roughness on the Magnetic Properties of Thin FCC Co Films," *Physical Review B* 76 (2007): 054429, https://doi.org/10.1103/PhysRevB.76.054429.

71. A. Gayen, G. K. Prasad, S. Mallik, S. Bedanta, and A. Perumal, "Effects of Composition, Thickness and Temperature on the Magnetic Properties of Amorphous CoFeB Thin Films," *Journal of Alloys and Compounds* 694 (2017): 823–832, https://doi.org/10.1016/j.jallcom.2016.10.066.

72. J. Holanda, O. Alves Santos, R. O. Cunha, et al., "Longitudinal Spin Seebeck Effect in Permalloy Separated From the Anomalous Nernst Effect: Theory and Experiment," *Physical Review B* 95 (2017): 214421, https://doi.org/10.1103/PhysRevB.95.214421.

73. J. Wang, J. K. Carson, M. F. North, and D. J. Cleland, "A New Approach to Modelling the Effective Thermal Conductivity of Heterogeneous Materials," *International Journal of Heat & Mass Transfer* 49 (2006): 3075–3083, https://doi.org/10.1016/j.ijheatmasstransfer.2006.02.007.

74. A. Suplicz, H. Hargitai, and J. G. Kovacs, "Methodology Development for Through-Plane Thermal Conductivity Prediction of Composites," *International Journal of Thermal Sciences* 100 (2016): 54–59, https://doi.org/10.1016/j.ijthermalsci.2015.09.012.

75. R. Verma, A. Chatterjee, A. Mustafa, N. C. Shivaprakash, S. Kasthurirengan, and U. Behera, "Analytical Heat Conduction Model of a Composite Material Based on Complete Spatial Randomness of Filler in Base Matrix," *International Journal of Thermal Sciences* 118 (2017): 292–302, https://doi.org/10.1016/j.ijthermalsci.2017.04.018.

76. R. Mévrel, J.-C. Laizet, A. Azzopardi, et al., "Thermal Diffusivity and Conductivity of Zr 1−X Y X O 2−X/2 (x = 0, 0.084 and 0.179) Single Crystals," *Journal of the European Ceramic Society* 24 (2004): 3081–3089, https://doi.org/10.1016/j.jeurceramsoc.2003.10.045.

77. L. Fornarini, J. C. Conde, C. Alvani, D. Olevano, and S. Chiussi, "Experimental Determination of La_2O_3 Thermal Conductivity and Its Application to the Thermal Analysis of a-Ge/La_2O_3/c-Si Laser Annealing," *Thin Solid Films* 516 (2008): 7400–7405, https://doi.org/10.1016/j.tsf.2008.02.032.

78. S. A. de Oliveira, R. T. Doumbi, A. de Morais, et al., "Experimental and Theoretical Approaches for Thermomagnetic Properties of CoFe-Based Flexible Amorphous Ribbons: Shape Anisotropy Contribution," *Journal of Magnetism and Magnetic Materials* 638 (2026): 173738, https://doi.org/10.1016/j.jmmm.2025.173738.

Supporting Information

Additional supporting information can be found online in the Supporting Information section.

Supporting File: jace70907-sup-0001-SuppMat.docx.